Three-dimensional biventricular strains in pulmonary arterial hypertension patients using hyperelastic warping

Hua Zou, Shuang Leng, Ce Xi, Xiaodan Zhao, Angela S Koh, Fei Gao, Ju Le Tan, Ru-San y Tan, John C Allen, Lik Chuan Lee, et al.

Three-dimensional biventricular strains in pulmonary arterial hypertension patients using hyperelastic warping

Hua Zou[a], Shuang Leng[a], Ce Xi[b], Xiaodan Zhao[a], Angela S Koh[a,c], Fei Gao[a], Ju Le Tan[a,c], Ru-San Tan[a,c], John C Allen[c], Lik Chuan Lee[b], Martin Genet[d,e], Liang Zhong[a,c,*]

[a]National Heart Research Institute Singapore, National Heart Centre Singapore, Singapore

[b]Department of Mechanical Engineering, Michigan State University, MI, United States

[c]Duke-NUS Medical School, Singapore

[d]Mechanics Department & Solid Mechanics Laboratory, École Polytechnique (Paris-Saclay University), Palaiseau, France

[e]M3DISIM research team, INRIA (Paris-Saclay University), Palaiseau, France

*Correspondence: Dr. Liang Zhong

Address: National Heart Centre Singapore, 5 Hospital Drive, 169609, Singapore

Email: zhong.liang@nhcs.com.sg; Phone: +6567042237

Abstract

Background and Objective: Evaluation of biventricular function is an essential component of clinical management in pulmonary arterial hypertension (PAH). This study aims to examine the utility of biventricular strains derived from a model-to-image registration technique in PAH patients in comparison to age- and gender-matched normal controls.

Methods: A three-dimensional (3D) model was reconstructed from cine short- and long-axis cardiac magnetic resonance (CMR) images and subsequently partitioned into right ventricle (RV), left ventricle (LV) and septum. The hyperelastic warping method was used to register the meshed biventricular finite element model throughout the cardiac cycle and obtain the corresponding biventricular circumferential, longitudinal and radial strains.

Results: Intra- and inter-observer reproducibility of biventricular strains was excellent with all intra-class correlation coefficients > 0.84. 3D biventricular longitudinal, circumferential and radial strains for RV, LV and septum were significantly decreased in PAH patients compared with controls. Receiver operating characteristic (ROC) analysis showed that the 3D biventricular strains were better early markers (Area under the ROC curve = 0.96 for RV longitudinal strain) of ventricular dysfunction than conventional parameters such as two-dimensional strains and ejection fraction.

Conclusions: Our highly reproducible methodology holds potential for extending CMR imaging to characterize 3D biventricular strains, eventually leading to deeper understanding of biventricular mechanics in PAH.

Keywords: Biventricular strain, Cardiac magnetic resonance, Hyperelastic warping, Pulmonary arterial hypertension

1. Introduction

Pulmonary arterial hypertension (PAH) is a progressive disorder characterized by elevated pulmonary artery pressure (PAP) and pulmonary artery vascular resistance, leading to right ventricular (RV) dysfunction and ultimately right-sided heart failure [1]. PAP measurement by right heart catheterization is the current gold standard for PAH [2], but it is invasive. Echocardiography is the modality of choice in evaluating PAH because of its availability and low cost, and three-dimensional (3D) echocardiography (3DE) is one technique that can be used to quantify RV volumes and strains. However, the RV endocardial surface is sometimes difficult to discern by 3DE, owing to the abundance of aberrant papillary muscles. The fibrous trabecular network is highly echogenic and appears as a solid muscular layer, causing little differentiation between RV myocardium and trabeculae. As a consequence, RV volume is usually underestimated by 3DE compared with cardiac magnetic resonance (CMR) imaging [3].

CMR has recently been considered as a potential one-stop-shop imaging modality in PAH [4]. It is the gold standard for measuring ventricular ejection fraction (EF), volume and mass. It is also widely used to quantify ventricular curvedness, deformation, systolic and diastolic function [5-9] as well as in vivo myocardial properties through inverse finite element modelling [10,11] in many heart diseases. Due to its high resolution, motion tracking can be performed over the cardiac cycle. Most motion tracking methods aim to extract strains in the heart, as myocardial strain presents the basic mechanical function of the myocardium and has the potential to become an important clinical index of the regional ventricular function. Myocardial strains are widely computed in radial, longitudinal and circumferential directions [12]. Longitudinal strain is the main strain component in the assessment of the RV function. It has been found to be significantly associated with hemodynamic parameters of RV function [13] and may represent a useful prognostic marker in patients with PAH [14].

The hyperelastic warping method is a deformable image registration technique used to estimate strain from medical images. Veress et al. [15] proposed a hyperelastic warping method to determine left ventricular (LV) strain from mid-diastole to end-diastole using multiple short-axis slices from CMR images. In the hyperelastic warping method, a finite element model of the region of interest is deformed by a body force that depends on the difference of image intensities between the template image and the target image. A hyperelastic strain energy function is applied to constrain and regularize the deformation [16,17]. Other regularizers have also been proposed, such as incompressibility [18], equilibrium gap [19-21], knowledge based reconstruction [22,23], and D-Affine regularization [24,25]. Application of the hyperelastic warping method in cardiac motion and function has focused primarily on quantifying LV strains [26,27], that has been verified using strains computed from tagged CMR [28] and 3D complementary spatial modulation of magnetization (CSPAMM) CMR images [17]. This method has also been applied to quantify circumferential strain in individual patient with heart failure with preserved ejection fraction [29,30] and PAH [31].

Here, we aim to quantify the 3D biventricular circumferential, longitudinal and radial strains in PAH patients and normal controls using the hyperelastic warping method. The goals of the presented study were as follows: (1) to examine the utility of biventricular 3D strains derived from a model-to-image registration technique in PAH patients in comparison to age- and gender-matched normal controls; (2) to evaluate the reproducibility of the technique; (3) to investigate the abnormalities in RV, LV and septum strains and interventricular interactions of PAH patients; and (4) to compare the 3D strains with conventional two-dimensional (2D) stains from feature tracking.

2. Methods

2.1 Study population

PAH patients were recruited from the prospective studies of 3D curvedness-base imaging (ClinicalTrials.gov Identifier: NCT02790918) and right heart mechanics in congenital heart diseases (ClinicalTrials.gov Identifier: NCT03217240). In addition, 17 age- and gender-matched normal controls without known cardiovascular disease or other co-morbidities were consecutively selected from our healthy subject database. All subjects underwent CMR scans. The protocol was approved by the SingHealth Centralised Institutional Review Board. Informed consents were obtained from all subjects. The study protocol conforms to the ethical guidelines of the 1975 Declaration of Helsinki.

2.2 CMR image acquisition

CMR scans were conducted using steady-state free precession (SSFP) cine gradient echo sequences in a 3 T Philips scanner (Ingenia, Philips Healthcare, The Netherlands) with a 12-element body matrix coil. SSFP end-expiratory breath-hold cine images were acquired in multi-planar short- (from apex to basal) and long-axis views (2-, 3-, 4-chamber views, Fig. 1). Typical imaging parameters were: TR/TE 3/1 ms, flip angle 45°, slice thickness 8 mm, pixel bandwidth 1796 Hz, field of view 300×300 mm^2, temporal resolution ~35 ms, in-plane spatial resolution 1.6×1.6 – 1.8×1.8 mm^2, 40/30 frames per cardiac cycle.

2.3 Right heart catheterization

Right heart catheterization was performed at rest using standard techniques. PAH was defined as having a mean pulmonary artery pressure of ≥25 mmHg; pulmonary artery wedge pressure of ≤15 mmHg; and pulmonary vascular resistance >3 Wood units. Invasive hemodynamic measurements were not available in the control group.

2.4 Overall framework of hyperelastic warping registration

The core of the method was based on the hyperelastic warping technique to register a meshed biventricular finite element model reconstructed from the CMR images at end-systole, with those acquired at other time points during a cardiac cycle, to track the motion of heart and obtain the corresponding strain-time curves. Short-axis images were used for registration. As there is an excursion in long-axis direction of the ventricle, we measured the displacement of septum manually, and assigned this displacement as a boundary condition in long-axis direction. The whole framework is illustrated in Fig. 2, and it was implemented using MeVisLab (MeVis Medical Solution AG, Bremen, Germany), VTK, Gmsh [32], FEniCS [33], and in-house code [17]. The following subsections explain each step in details.

2.4.1 Model reconstruction

Figure 3 shows the reconstruction of the model. Contours of the LV and RV endocardial, and whole heart epicardial surfaces were manually delineated in both short-axis and long-axis images in the end-systolic frame, as shown in Fig. 3(A). Contouring was performed on the full image stack associated with the end-systole time point as defined by the closure of the aortic valve [34]. Papillary muscles were excluded from the LV myocardium. 4∼9 short-axis images depending on the size of heart and the 4-chamber long-axis image were used for each subject. These contours were then used to reconstruct the LV endocardial surface, RV endocardial surface and whole heart epicardial surface, as shown in Fig. 3(B) and 3(C). Gmsh was used for generation of the meshes for each model, with a mesh size of 0.3, as shown in Fig. 3(D). The nodes of the models ranged from 2313∼3298, and the elements ranged from 7527∼11485. Each model was partitioned into three regions: LV, RV and septum, as shown in Fig. 3(E).

2.4.2 Image preparation and boundary condition assignment

Short-axis images were interpolated to double the number of short-axis slices for better registration, as the full short-axis image stack was sparse compared with the model. This step

was implemented using a Lanczos filter in MeVisLab. Meanwhile, excursion of the ventricles in the long-axis direction was measured, as shown in Fig. 4. A sinusoidal function of this displacement was imposed as a constraint in the biventricular model in the hyperelastic warping method.

2.4.3 Hyperelastic warping registration and post-processing of strains

Registration using hyperelastic warping and derivation of strains were detailed in our prior study [30]. In summary, the displacement field **U** relative to position **X** of the meshed volume **Ω** is derived from the difference in image intensity of a reference image *R* and a target image *T* by minimizing the following energy expression in hyperelastic warping:

$$\int W(\mathbf{X},\mathbf{U})d\Omega + \int \frac{\gamma}{2}\big(R(\mathbf{X}) - T(\mathbf{X}+\mathbf{U})\big)^2 d\Omega$$

Here, a Neo-Hookean strain energy function is used to define the hyperelastic strain energy *W*. γ is the penalty parameter enforcing the alignment of the reference image to the target image. Successive registration is done for different time points during a cardiac cycle.

The local Green-Lagrange strain tensor **E** is derived based on the deformation gradient **F**, which is defined as $\mathbf{F} = \frac{\partial(\mathbf{X}+\mathbf{U})}{\partial \mathbf{X}}$. Strain measurements in circumferential direction ε_{CC}, longitudinal direction ε_{LL}, and radial direction ε_{RR} are computed by projecting **E** onto these directions using $\varepsilon_{ii} = \mathbf{e_i} \cdot \mathbf{E}\mathbf{e_i}$ with $\boldsymbol{i} \in (C, L, R)$ [30]. $\mathbf{e}_C$, $\mathbf{e}_L$ and $\mathbf{e}_R$ were prescribed using the Laplace-Dirichlet rule-based (LDRB) algorithm [35].

Figure 5(A) shows the meshed model of three regions (LV, RV and septum) with the CMR images. Figure 5(B)-(G) present the circumferential, longitudinal and radial strain directions and strain-time curves for LV, RV and septum respectively.

2.5 2D strain estimation

2D circumferential, longitudinal and radial strains were measured using post-processing feature tracking software (Medis QStrain Software, Medis Medical Imaging Systems, version

2.0, Leiden, The Netherlands). For each subject, three short-axis (basal, middle and apex) images, and 4-chamber long-axis image were used. Figure 6 shows an example for circumferential strain tracked in a middle short-axis image. It is noted that septum strain can be calculated by averaging the strains in the septal segments (purple and yellow segments in Fig. 6), and LV wall strain can be obtained by averaging the four LV segments (green, white, light and dark blue segments in Fig. 6). After performing the analysis in three short-axis images, we averaged the strain measurements obtained in these three slices covering basal, middle and apex of the ventricle. RV strains were obtained with the same procedures. The 4-chamber long-axis image was used for measuring longitudinal strain.

2.6 Reproducibility

The inter- and intra-observer variability was assessed with randomly selected 8 cases including 4 controls and 4 PAH patients. The strain measurements from two independent observers (HZ and CX) were compared for inter-observer variability; and the same observer (HZ) re-analyzed the 8 cases, one month apart, for assessing the intra-observer variability.

2.7 Statistical analysis

Data was analysed using SPSS (version 17.0, Chicago, IL, USA). Comparisons between PAH patients and normal controls were performed using Mann-Whitney *U* tests. Receiver operating characteristic (ROC) analysis was conducted to assess the diagnostic performance of biventricular strain measurements. Intra- and inter-observer variability was assessed by mean bias±standard deviation (SD), limits of agreement, coefficient of variation (CV) and intra-class correlation coefficient (ICC). ICC $\geq$0.75 was considered excellent. $P<0.05$ was regarded as statistically significant.

3. Results

3.1. Patient demographics

A total of 34 human subjects including 17 PAH patients (mean age 47±16 years) and 17 age- and gender-matched normal controls (49±15 years) were enrolled in the study. The demographics of the study groups are summarized in Table 1. Compared to the normal controls, PAH patients had a comparable LVEF, but lower RVEF (42±12 vs. 60±6%, P<0.0001). RV end-diastolic volume (EDV) index and end-systolic volume (ESV) index were higher in PAH patients than controls (109±33 vs. 73±9 ml/m^2 and 65±29 vs. 30±7 ml/m^2 respectively, P<0.0001). PAH patients were comparable to controls with respect to LVEDV index, LVESV index, LV stroke volume (SV) index, and LV mass index. Heart rate of PAH patients was higher than controls (81±13 vs. 69±11, P=0.006). Invasive hemodynamic parameters are reported in Table 1 too.

3.2. Peak circumferential, longitudinal and radial strains

Table 2 shows the peak circumferential, longitudinal and radial strains in different regions (RV, LV and septum) for controls and PAH patients, respectively. PAH patients had significantly decreased RV circumferential (ε_{CC}^{RV}: -7.2±2.9 vs. -9.5±2.0%, P=0.011), longitudinal (ε_{LL}^{RV}: -10.0±3.0 vs. -15.4±1.6%, P<0.0001) and radial strains (ε_{RR}^{RV}: 15.8±7.2 vs. 26.1±6.5%, P<0.0001). LV strains were also significantly lower in PAH patients (ε_{CC}^{LV}: -11.8±2.7 vs. -14.7±1.8%, P=0.001; ε_{LL}^{LV}: -12.5±3.2 vs. -15.5±1.5%, P=0.002; ε_{RR}^{LV}: 26.9±12.4 vs. 35.9±7.8%, P=0.015) in comparison to normal controls. Septum strains in PAH patients were significantly lower than controls (ε_{CC}^{Sep}: -4.3±1.9 vs. -5.9±1.7%, P=0.015; ε_{LL}^{Sep}: -13.0±4.1 vs. -17.1±2.0%, P=0.001; ε_{RR}^{Sep}: 9.3±4.9 vs. 14.4±4.4%, P=0.004).

3.3. ROC analysis for PAH diagnosis

ROC analyses for strains, RVEF and LVEF were performed to differentiate PAH patients from controls, and results are shown in Table 3. RV longitudinal strain ε_{LL}^{RV} was the best

variable (Area under the ROC curve (AUC) = 0.958, Sensitivity = 88%, Specificity = 100%, threshold = -13.1%) compared to RVEF (AUC = 0.910, Sensitivity = 71%, Specificity = 94%, threshold = 50%) to distinguish PAH patients from normal controls.

3.4. Reproducibility

Table 4 shows the intra- and inter-observer variability for 8 randomly chosen cases (4 controls, 4 PAH). ε_{CC}^{LV} had the best intra-observer agreement (bias, 0.0±1.2%; limits of agreement, -2.3 to 2.3%) and ε_{LL}^{RV} had the best inter-observer agreement (bias, -0.9±0.9%; limits of agreement, -2.7 to 1.0%). In terms of ICC, all strains had an excellent intra- (ICC ≥0.91) and inter-observer (ICC ≥0.84) agreements.

3.5. Comparison with 2D strains

Results of 2D strains derived by feature tracking and correlations between 3D and 2D strains are listed in Table 5. Among the 2D strain measurements, RV longitudinal strain ε_{LL}^{RV}, septum longitudinal strain ε_{LL}^{Sep}, and septum radial strain ε_{RR}^{Sep} were significantly smaller in PAH patients than controls, while other strain components were comparable between patients and controls. Ranking of the correlations between 3D and 2D strains from strong to weak were as follows: ε_{RR}^{Sep} (R=0.65), ε_{CC}^{RV} (R=0.61), ε_{LL}^{Sep} (R=0.61), ε_{RR}^{LV} (R=0.47), ε_{CC}^{LV} (R=0.45), ε_{LL}^{RV} (R=0.44), (ε_{LL}^{LV}: R=0.32), ε_{CC}^{Sep} (R=0.30).

4. Discussions

Survival of patients with PAH is strongly related to RV function [36]. In PAH, RV free wall strain has emerged as an important predictor of the outcome [37]. In addition, LV performance may be affected because both ventricles share the interventricular septum within the same pericardial sac. Keeping this in mind, we investigated the 3D RV, LV and septum strains by treating the heart as a whole and studied the biventricular motion simultaneously.

4.1. RV strains

RV strains (ε_{CC}^{RV}, ε_{LL}^{RV} and ε_{RR}^{RV}) for PAH patients were significantly reduced compared to the controls, with ε_{LL}^{RV} being the best RV variable for diagnosis of PAH, demonstrating the comprehensive impairment in RV motion for this type of heart disease. There were significant positive correlations between RV strains (ε_{CC}^{RV}, ε_{LL}^{RV} and ε_{RR}^{RV}) and RVEF (R=0.70, 0.67 and 0.65, respectively, all P<0.0001). Architectural arrangement of muscle fibres in the RV differs from that in LV. In RV, the relatively thin wall is composed primarily of longitudinal fibres. This arrangement in RV may contribute to the predominantly longitudinal RV shortening responsible for blood ejection during systole [38], explaining the superior diagnostic performance of RV longitudinal strain ε_{LL}^{RV} and strongest correlation between ε_{LL}^{RV} and RVEF. Reductions in ε_{CC}^{RV} and ε_{RR}^{RV} in PAH patients may be due to circumferential stretch and subsequent impairment in contractility. Because the myocardium of RV free wall is oblique in the superficial submyocardium, this finding may signify the failure of outer layer to contract circumferentially [13]. CMR studies had highlighted the value of considering ε_{CC}^{RV} for some pathology such as arrhythmogenic RV cardiomyopathy or RV afterload changes [39]. Of note, radial strains in the RV and LV are less reported due to their poor reproducibility by conventional techniques. However, good intra- and inter-observer reproducibility for radial strains was achieved in current study.

4.2. Septum and LV strains

The finding that ε_{CC}^{Sep}, ε_{LL}^{Sep} and ε_{RR}^{Sep} were depressed in PAH patients is interesting and important. In a study by Querejeta Roca et al. [40], PAH was associated with impaired ε_{LL}^{RV} and ε_{CC}^{Sep}. Under normal circumstances, the septum behaves much like a thick-walled cylinder subjected to internal and external pressure, with the resulting stress being circumferentially tensile and radially compressive, just like the remainder of the LV [41]. In PAH, however,

increased trans-septal pressure gradient causes bowing of the interventricular septum towards the LV. The septum withstanding this pressure load becomes more flattened, and is threatened by substantial compressive wall stress, which impedes septal blood flow and affects septal performance [41]. Two studies on the finite element modelling can help us understand this physiology [42,43].

Our study also revealed that LV strains (ε_{CC}^{LV}, ε_{LL}^{LV} and ε_{RR}^{LV}) were significantly reduced in PAH patients compared to normal controls despite comparable LVEF, indicating the capabilities of LV strains as early markers of LV dysfunction in PAH. This is in consistent with the findings of Puwanant et al. [44], who found both ε_{CC}^{LV} and ε_{CC}^{Sep} were decreased in patients with pulmonary hypertension (PH). A potential explanation could be that a reverse septal curvature and more D-shaped LV in PAH patients would affect the myocardial fibre shortening and contraction.

4.3. Comparison with 2D strains

Moderate correlations between 3D and 2D strains were observed in most of the strain components (Table 5). For 2D strains, only ε_{LL}^{RV}, ε_{LL}^{Sep} and ε_{RR}^{Sep} had significant differences between PAH patients and controls. However, 3D strains revealed more abnormalities in RV, LV and septum (Table 2). As the 3D strain analysis involved the entire biventricular unit, it can better represent the interventricular interaction in this kind of heart disease. Actually, given the complex anatomy of the RV, circumferential strain cannot be fully assessed by 2D techniques [45]. On the other hand, most existing software systems are designed for the LV and the same algorithm for assessing the strain of RV may be sub-optimal.

4.4. Limitations and long-term prospects

There are limitations in this study, including relatively small number of enrolled subjects, the need for manual segmentation, and the lack of inflow and outflow tract geometry in the

biventricular model. Besides, longitudinal strain was calculated by imposing a basal longitudinal displacement assuming to vary sinusoidally with time. A higher out-of-plane resolution (smaller slice thickness) may obviate the need to impose such an assumption. Our study was designed for Group 1 PH patients (pre-capillary). In the future we may have another trial to look at reactive or Group 2 post-capillary PH patients that are patients with mean pulmonary artery pressure >25 mmHg, pulmonary artery wedge pressure >15 mmHg and pulmonary vascular resistance <3 Wood units. In addition, evaluation of the prognostic power of the motion models is warranted in future studies with larger data size [46]. Finally, the same technique may be applied in the atria to investigate the association between atrial dysfunction and disease progression in PAH [47] and heart failure [48].

5. Conclusions

The feasibility and effectiveness of the biventricular 3D strains using hyperelastic warping have been well demonstrated in current study. The biventricular strains appeared to be better early markers of RV and LV dysfunction in patients with PAH. Our highly reproducible methodology holds potential for extending CMR imaging to characterize 3D biventricular strains, eventually leading to deeper understanding of biventricular mechanics in PAH.

Acknowledgments

This research was supported in part by grants from the National Medical Research Council (NMRC/OFIRG/0018/2016; NMRC/BnB/0017/2015; NMRC HSRG-OC17Nov009; NMRC/TA0031/2015; MOH-000153), Biomedical Engineering Programme, Agency for Science, Technology and Research, Singapore Project Grant (132 148 0012), and the Biomedical Research Council (14/1/32/24/002), American Heart Association

(17SDG33370110, Lee), National Institutes of Health (R01 HL 134841-01A1, Lee). The protocol was approved by the SingHealth Centralised Institutional Review Board.

Conflict of interest statement

The authors have no conflicts of interest, financial or otherwise.

References

1. R. Naeije, A. Manes, *The right ventricle in pulmonary arterial hypertension*. Eur. Respir. Rev. 23 (2014) 476-487.
2. P. Callan, A.L. Clark, *Right heart catheterisation: indications and interpretation*. Heart. 102 (2016) 1-11.
3. H.B. Van Der Zwaan, M.L. Geleijnse, J.S. McGhie, E. Boersma, W.A. Helbing, F.J. Meijboom, J.W. Roos-Hesselink, *Right ventricular quantification in clinical practice: Two-dimensional vs. three-dimensional echocardiography compared with cardiac magnetic resonance imaging*. Eur. J. Echocardiogr. 12 (2011) 656-664.
4. W.M. Bradlow, J.S. R Gibbs, R.H. Mohiaddin, *Cardiovascular magnetic resonance in pulmonary hypertension*. J. Cardiovasc. Magn. Reson. 14 (2012) 6.
5. L. Zhong, L. Gobeawan, Y. Su, J.L. Tan, D. Ghista, T. Chua, R.-S. Tan, G. Kassab. *Right ventricular regional wall curvedness and area strain in patients with repaired tetralogy of Fallot*. Am. J. Physiol. Heart Circ. Physiol. 302 (2012) H1306-H1316.
6. L. Zhong, Y. Su, S.-Y. Yeo, R.-S. Tan, D. Ghista, G. Kassab, *Left ventricular regional wall curvedness and wall stress in patients with ischemic dilated cardiomyopathy*. Am. J. Physiol. Heart Circ. Physiol. 296 (2009) H573-H584.
7. S. Leng, M. Jiang, X.D. Zhao, J.C. Allen, G. Kassab, R.Z. Ouyang, J.L Tan, B. He, R.-S. Tan, L. Zhong, *Three-dimensional tricuspid annular motion analysis from cardiac magnetic resonance feature-tracking*. Ann. Biomed. Eng. 44 (2016) 3522-3538.
8. S. Leng, X.D. Zhao, F.Q. Huang, J.I. Wong, B.Y. Su, J.C. Allen, G. Kassab, R.-S. Tan, L. Zhong, *Automated quantitative assessment of cardiovascular magnetic resonance-derived atrioventricular junction velocities*. Am. J. Physiol. Heart Circ. Physiol. 309 (2015) H1923-H1935.

9. S. Leng, S. Zhang, M. Jiang, X.D. Zhao, R. Wu, J.C. Allen, B. He, R.-S. Tan, L. Zhong, *Imaging 4D morphology and dynamics of mitral annulus in humans using cardiac cine MR feature tracking*. Sci. Rep. 8 (2018) 81.
10. L.C. Lee, L. Ge, Z. Zhang, M. Pease, S.D. Nikolic, R. Mishra, M.B. Ratcliffe, J.M. Guccione, *Patient-specific finite element modeling of the Cardiokinetix Parachute device: Effects on left ventricular wall stress and function*. Med. Biol. Eng. Comput. 52 (2014) 557-566.
11. M. Genet, L.C. Lee, L. Ge, G. Acevedo-Bolton, N. Jeung, A. Martin, N. Cambronero, A. Boyle, Y. Yeghiazarians, S. Kozerke, J.M. Guccione, *A novel method for quantifying smooth regional variations in myocardial contractility within an infarcted human left ventricle based on delay-enhanced magnetic resonance imaging*. J. Biomech. Eng. 137 (2015) 081009.
12. H. Wang, A.A. Amini, *Cardiac motion and deformation recovery from MRI : A review*. IEEE Trans. Med. Imaging. 31 (2012) 487-503.
13. B.C. Smith, G. Dobson, D. Dawson, A. Charalampopoulos, J. Grapsa, P. Nihoyannopoulos, *Three-dimensional speckle tracking of the right ventricle: toward optimal quantification of right ventricular dysfunction in pulmonary hypertension*, J. Am. Coll. Cardiol. 64 (2014) 41-51.
14. M.E.M. de Siqueira, E. Pozo, V.R. Fernandes, P.P. Sengupta, K. Modesto, S.S. Gupta, C. Barbeito-Caamaño, J. Narula, V. Fuster, A. Caixeta, J. Sanz, *Characterization and clinical significance of right ventricular mechanics in pulmonary hypertension evaluated with cardiovascular magnetic resonance feature tracking*. J. Cardiovasc. Magn. Reson. 18 (2016) 39.

15. A.I. Veress, J.A. Weiss, G.J. Klein, G.T. Gullberg, L. Berkeley, *Quantification of 3D left ventricular deformation using hyperelastic warping : Comparisons between MRI and PET imaging*. Comput. Cardiol. (2002) 709-712.
16. A.I. Veress, G.T. Gullberg, J.A. Weiss, *Measurement of strain in the left ventricle with cine-MRI and deformable image registration*. J. Biomech. Eng. 127 (2005) 1195-1207.
17. M. Genet, C.T. Stoeck, C. von Deuster, L.C. Lee, J.M. Guccione, S. Kozerke, *Finite element digital image correlation for cardiac strain analysis from accelerated 3D whole-heart tagging*. in: Proceedings of the 24th Annual Meeting of ISMRM, 2016.
18. T. Mansi, X. Pennec, M. Sermesant, H. Delingette, N. Ayache, *ILogDemons: A demons-based registration algorithm for tracking incompressible elastic biological tissues*. Int. J. Comput. Vis. 92 (2011) 92-111.
19. M. Genet, L.C. Lee, S. Kozerke, *A continuum formulation of the finite strain equilibrium gap regularizer for finite element image correlation problems*. in: Proceedings of the 13e Colloque National en Calcul des Structures, 2017, pp. 13-17.
20. D. Claire, F. Hild, S. Roux, *A finite element formulation to identify damage fields: The equilibrium gap method*. Int. J. Numer. Methods Eng. 61 (2004) 189-208.
21. M. Genet, C.T. Stoeck, C. von Deuster, L.C. Lee, S. Kozerke, *Equilibrated warping: Finite element image registration with finite strain equilibrium gap regularization*. Med. Image Anal. 50 (2018) 1-22.
22. F.H. Sheehan, S. Ge, G.W. Vick, K. Urnes, W.S. Kerwin, E.L. Bolson, T. Chung, J.P. Kovalchin, D.J. Sahn, M. Jerosch-Herold, A.H. Stolpen, *Three-dimensional shape analysis of right ventricular remodeling in repaired tetralogy of Fallot*. Am. J. Cardiol. 101 (2008) 107-113.
23. M. Morcos, F.H. Sheehan, *Regional right ventricular wall motion in tetralogy of Fallot: A three dimensional analysis*. Int. J. Cardiovasc. Imaging. 29 (2013) 1051-1058.

24. K. Gilbert, B. Pontre, C.J. Occleshaw, B.R. Cowan, A. Suinesiaputra, A.A. Young, *4D modelling for rapid assessment of biventricular function in congenital heart disease*. Int. J. Cardiovasc. Imaging. 34 (2018) 407-417.
25. K. Gilbert, H.I. Lam, B. Pontré, B.R. Cowan, C.J. Occleshaw, J.Y. Liu, A.A. Young, *An interactive tool for rapid biventricular analysis of congenital heart disease*. Clin. Physiol. Funct. Imaging. 37 (2017) 413-420.
26. A.I. Veress, J.A. Weiss, R.H. Huesman, B.W. Reutter, E. Scott, A. Sitek, B. Feng, Y. Yang, G.T. Gullberg, *Measuring regional changes in the diastolic deformation of the left ventricle of SHR rats using microPET technology and hyperelastic warping*. Ann. Biomed. Eng. 36 (2008) 1104-1117.
27. A.I. Veress, G. Klein, G.T. Gullberg, *A comparison of hyperelastic warping of PET images with tagged MRI for the analysis of cardiac deformation*. Int. J. Biomed. Imaging. 2013 (2013).
28. N.S. Phatak, S.A. Maas, A.I. Veress, N.A. Pack, E.V.R. Di Bellaa, J.A. Weissa, *Strain measurement in the left ventricle during systole with deformable image registration*. Med. Image. Anal. 13 (2009) 354-361.
29. H. Zou, X.D. Zhao, C. Xi, L.C. Lee, M. Genet, Y. Su, R.-S. Tan, L. Zhong, *Characterization of patient-specific biventricular mechanics in heart failure with preserved ejection fraction: hyperelastic warping*. in: Proceedings of the 38th Annual International Conference of the IEEE Engineering in Medicine and Biology Society (EMBC), 2016, pp. 4149-4152.
30. H. Zou, C. Xi, X.D. Zhao, A.S. Koh, F. Gao, Y. Su, R.-S. Tan, J.C. Allen, L.C. Lee, M. Genet, L. Zhong, *Quantification of biventricular strains in heart failure with preserved ejection fraction patient using hyperelastic warping method*. Front. Physiol. 9 (2018) 1295.

31. C. Xi, C. Latnie, X.D. Zhao, J.L Tan, S.T. Wall, M. Genet, L. Zhong, L.C. Lee, *Patient-specific computational analysis of ventricular mechanics in pulmonary arterial hypertension*. J. Biomech. Eng. 138 (2016) 1-9.

32. C. Geuzaine, J.F. Remacle, *Gmsh: A 3-D finite element mesh generator with built-in pre- and post-processing facilities*. Int. J. Numer. Methods Eng. 79 (2009) 1309-1331.

33. M.S. Alnaes, J. Blechta, J. Hake, A. Johansson, B. Kehlet, A. Logg, C. Richardson, J. Ring, M.E. Rognes, G.N. Wells, *The FEniCS Project Version 1.5*. Arch. Numer. Softw. 3 (2015) 9-23.

34. J. Schulz-Menger, D.A. Bluemke, J. Bremerich, S.D. Flamm, M.A. Fogel, M.G. Friedrich, R.J. Kim, F. von Knobelsdorff-Brenkenhoff, C.M. Kramer, D.J. Pennell, S. Plein, E. Nagel, *Standardized image interpretation and post processing in cardiovascular magnetic resonance: Society for Cardiovascular Magnetic Resonance (SCMR) Board of Trustees Task Force on Standardized Post Processing*. J. Cardiovasc. Magn. Reson. 15 (2013) 35.

35. J.D. Bayer, R.C. Blake, G. Plank, N.A. Trayanova, *A novel rule-based algorithm for assigning myocardial fiber orientation to computational heart models*. Ann. Biomed. Eng. 40 (2012) 2243-2254.

36. T.M. Gorter, T.P. Willems, J.P. Van Melle, *Ventricular interdependence in pulmonary arterial hypertension: Providing small pieces of a complex puzzle*. Eur. J. Heart Fail. 17 (2015) 1-2.

37. N.M. Fine, L. Chen, P.M. Bastiansen, R.P. Frantz, P.A. Pellikka, J.K. Oh, G.C. Kane. *Outcome prediction by quantitative right ventricular function assessment in 575 subjects evaluated for pulmonary hypertension*. Circ. Cardiovasc. Imaging. 6 (2013) 711-721.

38. S.Y. Ho, P. Nihoyannopoulos, *Anatomy, echocardiography, and normal right ventricular dimensions*. Heart. 92 (2006) i2-i13.

39. E.J. Cho, P. Jiamsripong, A.M. Calleja, M.S. Alharthi, E.M. McMahon, B.K. Khandheria, M. Belohlavek, *Right ventricular free wall circumferential strain reflects graded elevation in acute right ventricular afterload*. Am. J. Physiol. Heart Circ. Physiol. 296 (2009) H413-H420.

40. G. Querejeta Roca, P. Campbell, B. Claggett, A. Vazir, D. Quinn, S.D. Solomon, A.M. Shah, *Impact of lowering pulmonary vascular resistance on right and left ventricular deformation in pulmonary arterial hypertension*. Eur. J. Heart Fail. 17 (2015) 63-73.

41. G.S. Nelson, E.Y. Sayed-Ahmed, H.E. ter Keurs, J.V. Tyberg, N.G. Shrive, *A 2D finite element model of the interventricular septum under normal and abnormal loading*. Comput. Methods Biomech. Biomed. Engin. 4 (2001) 307-322.

42. G.S. Nelson, E.Y. Sayed-Ahmed, C.A. Kroeker, Y.H. Sun, H.E. Keurs, N.G. Shrive, J.V. Tyberg, *Compression of interventricular septum during right ventricular pressure loading*. Am. J. Physiol. Heart Circ. Physiol. 280 (2001) H2639-H2648.

43. C.A. Gibbons Kroeker, S. Adeeb, J.V. Tyberg, N.G. Shrive, *A 2D FE model of the heart demonstrates the role of the pericardium in ventricular deformation*. Am. J. Physiol. Heart Circ. Physiol. 291 (2006) H2229-H2236.

44. S. Puwanant, M. Park, Z.B. Popović, W.H. Tang, S. Farha, D. George, J. Sharp, J. Puntawangkoon, J.E. Loyd, S.C. Erzurum, J.D. Thomas, *Ventricular geometry, strain, and rotational mechanics in pulmonary hypertension*. Circulation, 121 (2010) 259-266.

45. P. Moceri, N. Duchateau, D. Baudouy, E.D. Schouver, S. Leroy, F. Squara, E. Ferrari, M. Sermesant, *Three-dimensional right-ventricular regional deformation and survival in pulmonary hypertension*. Eur. Heart J. Cardiovasc. Imaging, 19 (2018) 450-458.

46. G.A. Bello, T.J.W. Dawes, J. Duan, C. Biffi, A. de Marvao, L.S.G.E. Howard, J.S.R. Gibbs, M.R. Wilkins, S.A. Cook, D. Rueckert, D.P. O'Regan, *Deep learning cardiac motion analysis for human survival prediction*. Nat. Mach. Intell. 1 (2019) 95-104.

47. S. Leng, Y. Dong, Y. Wu, X.D. Zhao, W. Ruan, G.C. Zhang, J.C. Allen, A.S. Koh, R.-S. Tan, J.W. Yip, J.L. Tan, Y.C. Chen, L. Zhong, *Impaired CMR-derived rapid semi-automated right atrial longitudinal strain is associated with decompensated hemodynamics in pulmonary arterial hypertension*. Circ. Cardiovasc. Imaging. 12 (2019) e008582.
48. S. Leng, R.-S. Tan, X.D. Zhao, J.C. Allen, A.S. Koh, L. Zhong, *Validation of a rapid semi-automated method to assess left atrial longitudinal phasic strains on cine cardiovascular magnetic resonance imaging*. J. Cardiovasc. Magn. Reson. 20 (2018) 71.

Figure legends

Figure 1. CMR images including short-axis images from apex to basal, and 2-, 3- and 4-chamber long-axis images.

Figure 2. Overall framework of quantifying the biventricular circumferential, longitudinal and radial strains.

Figure 3. Reconstruction of biventricular mesh: (A) segmentation of contours of LV, RV and septum; (B) Surface reconstruction; (C) Biventricular geometry (D) Biventricular mesh; (E) Partition of region (Red: right ventricle; Green: septum; Blue: left ventricle).

Figure 4. Measurement of the septal displacement in 4-chamber view as the boundary condition: (A) End-systole; (B) End-diastole; (C) Apply the displacement of septal on the model.

Figure 5. Registration of the meshed model with images for strain-time curves (A) meshed model with CMR image; (B) circumferential strain orientation; (C) circumferential strain-time curve; (D) longitudinal strain orientation; (E) longitudinal strain-time curve; (F) radial strain orientation; (G) radial strain-time curve.

Figure 6. Regional circumferential strain for middle short-axis slice by two-dimensional feature tracking.

Table 1. Baseline demographic and CMR characteristics of PAH patients and controls. The control group did not undergo right heart catheterization.

Variables	**Control (n = 17)**	**PAH (n = 17)**	***P* value**
Demographics			
Age, years	49±15	47±16	0.793
Gender, Male/Female	4/13	4/13	1.000
Weight, kg	59±12	58±12	0.762
Height, cm	159±10	161±12	0.723
Clinical Exam			
Body surface area, m^2	1.61 ± 0.20	1.60±0.21	0.889
Body mass index, kg/m^2	23.1±3.2	22.2±2.9	0.410
6 mins walking test, m	N/A	412±152	N/A
NT-ProBNP, pg/ml	N/A	1373±1885	N/A
NYHA functional class I, n	N/A	6	N/A
NYHA functional class II, n	N/A	9	N/A
NYHA functional class III, n	N/A	2	N/A
Cardiac magnetic resonance			
LVEF, %	65±6	61±10	0.183
LVEDV index, ml/m^2	70±7	70±26	0.956
LVESV index, ml/m^2	25±6	28±15	0.386
LVSV index, ml/m^2	45±4	42±13	0.383
LV mass index, g/m^2	38±9	45±15	0.116
RVEF, %	60±6	42±12	<0.0001
RVEDV index, ml/m^2	73±9	109±33	<0.0001
RVESV index, ml/m^2	30±7	65±29	<0.0001
RVSV index, ml/m^2	44±5	43±14	0.973
Hemodynamics			
Heart rate, bpm	69±11	81±13	0.006
Diastolic blood pressure, mmHg	76±12	76±15	0.932
Systolic blood pressure, mmHg	131±26	124±20	0.385
Cardiac output, l/min	N/A	4.4±2.2	N/A
Cardiac index, $l/min/m^2$	N/A	2.7±1.1	N/A
Right atrial pressure, mmHg	N/A	8.3±7.5	N/A
Mean pulmonary artery pressure, mmHg	N/A	45.8±15.2	N/A
Pulmonary capillary wedge pressure, mmHg	N/A	12.8±6.5	N/A
Pulmonary vascular resistance, Wood units	N/A	9.8±6.4	N/A

Data are mean±SD. NT-ProBNP: N-terminal pro b-type natriuretic peptide; NYHA: New York Heart Association; LV: left ventricular; EF: ejection fraction; EDV: end-diastolic volume; ESV: end-systolic volume; SV: stroke volume; RV: right ventricular; N/A: not applicable.

Table 2. Peak circumferential, longitudinal and radial strains in RV, LV and septum.

Variables	Control (n = 17)	PAH (n = 17)	*P* value
Right ventricular myocardial strain			
ε_{CC}^{RV}, %	-9.5±2.0	-7.2±2.9	0.011
ε_{LL}^{RV}, %	-15.4±1.6	-10.0±3.0	<0.0001
ε_{RR}^{RV}, %	26.1±6.5	15.8±7.2	<0.0001
Left ventricular myocardial strain			
ε_{CC}^{LV}, %	-14.7±1.8	-11.8±2.7	0.001
ε_{LL}^{LV}, %	-15.5±1.5	-12.5±3.2	0.002
ε_{RR}^{LV}, %	35.9±7.8	26.9±12.4	0.015
Septum myocardial strain			
ε_{CC}^{Sep}, %	-5.9±1.7	-4.3±1.9	0.015
ε_{LL}^{Sep}, %	-17.1±2.0	-13.0±4.1	0.001
ε_{RR}^{Sep}, %	14.4±4.4	9.3±4.9	0.004

Data are mean±SD. ε_{CC}^{RV}: right ventricular peak circumferential strain; ε_{LL}^{RV}: right ventricular peak longitudinal strain; ε_{RR}^{RV}: right ventricular peak radial strain; ε_{CC}^{LV}: left ventricular peak circumferential strain; ε_{LL}^{LV}: left ventricular peak longitudinal strain; ε_{RR}^{LV}: left ventricular peak radial strain; ε_{CC}^{Sep}: septum peak circumferential strain; ε_{LL}^{Sep}: septum peak longitudinal strain; ε_{RR}^{Sep}: septum peak radial strain; PAH: pulmonary arterial hypertension.

Table 3. AUC, sensitivity, specificity and threshold of the strains, RVEF and LVEF for differentiating PAH patients from normal controls.

Variables	**AUC**	**Sensitivity**	**Specificity**	**Threshold**
ε_{LL}^{RV}, %	0.958	88	100	-13.1
RVEF, %	0.910	71	94	50
ε_{RR}^{RV}, %	0.848	82	88	19.42
ε_{LL}^{Sep}, %	0.827	71	82	-15.4
ε_{LL}^{LV}, %	0.820	88	71	-15.1
ε_{CC}^{LV}, %	0.796	65	88	-13.2
ε_{RR}^{Sep}, %	0.782	65	88	9.8
ε_{CC}^{Sep}, %	0.765	82	82	-5.0
ε_{RR}^{LV}, %	0.758	77	76	31.1
ε_{CC}^{RV}, %	0.744	77	65	-8.8
LVEF, %	0.467	71	47	65

AUC: area under the receiver operating characteristic curve; ε_{LL}^{RV}: right ventricular peak longitudinal strain; RV: right ventricular; EF: ejection fraction; ε_{RR}^{RV}: right ventricular peak radial strain; ε_{LL}^{Sep}: septum peak longitudinal strain; ε_{LL}^{LV}: left ventricular peak longitudinal strain; ε_{CC}^{LV}: left ventricular peak circumferential strain; ε_{RR}^{Sep}: septum peak radial strain; ε_{CC}^{Sep}: septum peak circumferential strain; ε_{RR}^{LV}: left ventricular peak radial strain; ε_{CC}^{RV}: right ventricular peak circumferential strain; LV: left ventricular.

Table 4. Inter- and intra-observer reproducibility for 8 randomly chosen cases (4 PAH, 4 normal controls).

Variables	Variability	Mean bias±SD	Limits of agreement	CV (%)	ICC (95% CI)
ε_{CC}^{RV}	Intra-observer	0.5±0.9	-1.3 to 2.4	8.1	0.91 (0.55, 0.98)
	Inter-observer	0.9±0.7	-0.5 to 2.3	8.5	0.96 (0.80, 0.99)
ε_{CC}^{LV}	Intra-observer	0.0±1.2	-2.3 to 2.3	5.9	0.92 (0.60, 0.98)
	Inter-observer	1.3±0.9	-0.5 to 3.2	8.0	0.96 (0.81, 0.99)
ε_{CC}^{Sep}	Intra-observer	0.2±0.9	-2.0 to 1.6	11.4	0.94 (0.81, 0.99)
	Inter-observer	0.5±0.9	-1.3 to 2.3	12.7	0.94 (0.72, 0.99)
ε_{LL}^{RV}	Intra-observer	0.1±1.3	-2.4 to 2.6	6.4	0.97 (0.93, 0.99)
	Inter-observer	-0.9±0.9	-2.7 to 1.0	7.0	0.98 (0.90, 1.00)
ε_{LL}^{LV}	Intra-observer	-0.2±1.4	-2.9 to 2.5	6.1	0.95 (0.75, 0.99)
	Inter-observer	1.6±1.3	-0.9 to 4.2	6.8	0.89 (0.44, 0.98)
ε_{LL}^{Sep}	Intra-observer	-0.1±1.5	-3.2 to 2.9	6.7	0.95 (0.77, 0.99)
	Inter-observer	-0.6±1.6	-3.6 to 2.5	7.5	0.94 (0.71, 0.99)
ε_{RR}^{RV}	Intra-observer	-1.0±2.9	-6.7 to 4.6	8.7	0.98 (0.92, 1.00)
	Inter-observer	-0.6±2.2	-3.7 to 4.9	7.1	0.99 (0.93, 1.00)
ε_{RR}^{LV}	Intra-observer	-0.8±5.0	-10.6 to 9.0	10.7	0.97 (0.84, 0.99)
	Inter-observer	-2.3±6.0	-14.0 to 9.4	14.5	0.84 (0.21, 0.97)
ε_{RR}^{Sep}	Intra-observer	0.7±1.9	-2.9 to 4.4	10.4	0.98 (0.89, 1.00)
	Inter-observer	-0.6±1.4	-3.3 to 2.2	8.5	0.98 (0.92, 1.00)

ε_{CC}^{RV}: right ventricular peak circumferential strain; ε_{CC}^{LV}: left ventricular peak circumferential strain; ε_{CC}^{Sep}: septum peak circumferential strain. ε_{LL}^{RV}: right ventricular peak longitudinal strain; ε_{LL}^{LV}: left ventricular peak longitudinal strain; ε_{LL}^{Sep}: septum peak longitudinal strain; ε_{RR}^{RV}: right ventricular peak radial strain; ε_{RR}^{LV}: left ventricular peak radial strain; ε_{RR}^{Sep}: septum peak radial strain; SD: standard deviation; CV: coefficient of variation; ICC: intra-class correlation coefficient; CI: confidence interval.

Table 5. 2D Circumferential, longitudinal and radial strains by feature tracking and comparisons with 3D strains.

Variables	PAH (n = 17)	Control (n = 17)	*P* value PAH vs. Control	Pearson's Correlation (2D vs. 3D strains)
ε_{CC}^{RV}, %	-10.0±6.4	-13.3±2.8	0.067	0.61 (*P*<0.0001)
ε_{LL}^{RV}, %	-18.3±7.8	-24.3±7.6	0.030	0.44 (*P*=0.009)
ε_{RR}^{RV}, %	34.9±12.6	34.3±19.9	0.917	-0.16 (*P*=0.379)
ε_{CC}^{LV}, %	-19.4±4.5	-21.0±3.6	0.272	0.45 (*P*=0.007)
ε_{LL}^{LV}, %	-21.7±3.5	-22.1±3.9	0.750	0.32 (*P*=0.067)
ε_{RR}^{LV}, %	57.7±26.4	64.2±26.9	0.477	0.47 (*P*=0.005)
ε_{CC}^{Sep}, %	-15.3±3.7	-17.0±4.3	0.229	0.30 (*P*=0.082)
ε_{LL}^{Sep}, %	-11.7±5.9	-19.6±3.4	<0.0001	0.61 (*P*<0.0001)
ε_{RR}^{Sep}, %	34.7±15.2	46.3±16.8	0.043	0.65 (*P*<0.0001)

ε_{CC}^{RV}: right ventricular peak circumferential strain; ε_{LL}^{RV}: right ventricular peak longitudinal strain; ε_{RR}^{RV}: right ventricular peak radial strain; ε_{CC}^{LV}: left ventricular peak circumferential strain; ε_{LL}^{LV}: left ventricular peak longitudinal strain; ε_{RR}^{LV}: left ventricular peak radial strain; ε_{CC}^{Sep}: septum peak circumferential strain; ε_{LL}^{Sep}: septum peak longitudinal strain; ε_{RR}^{Sep}: septum peak radial strain; PAH: pulmonary arterial hypertension.

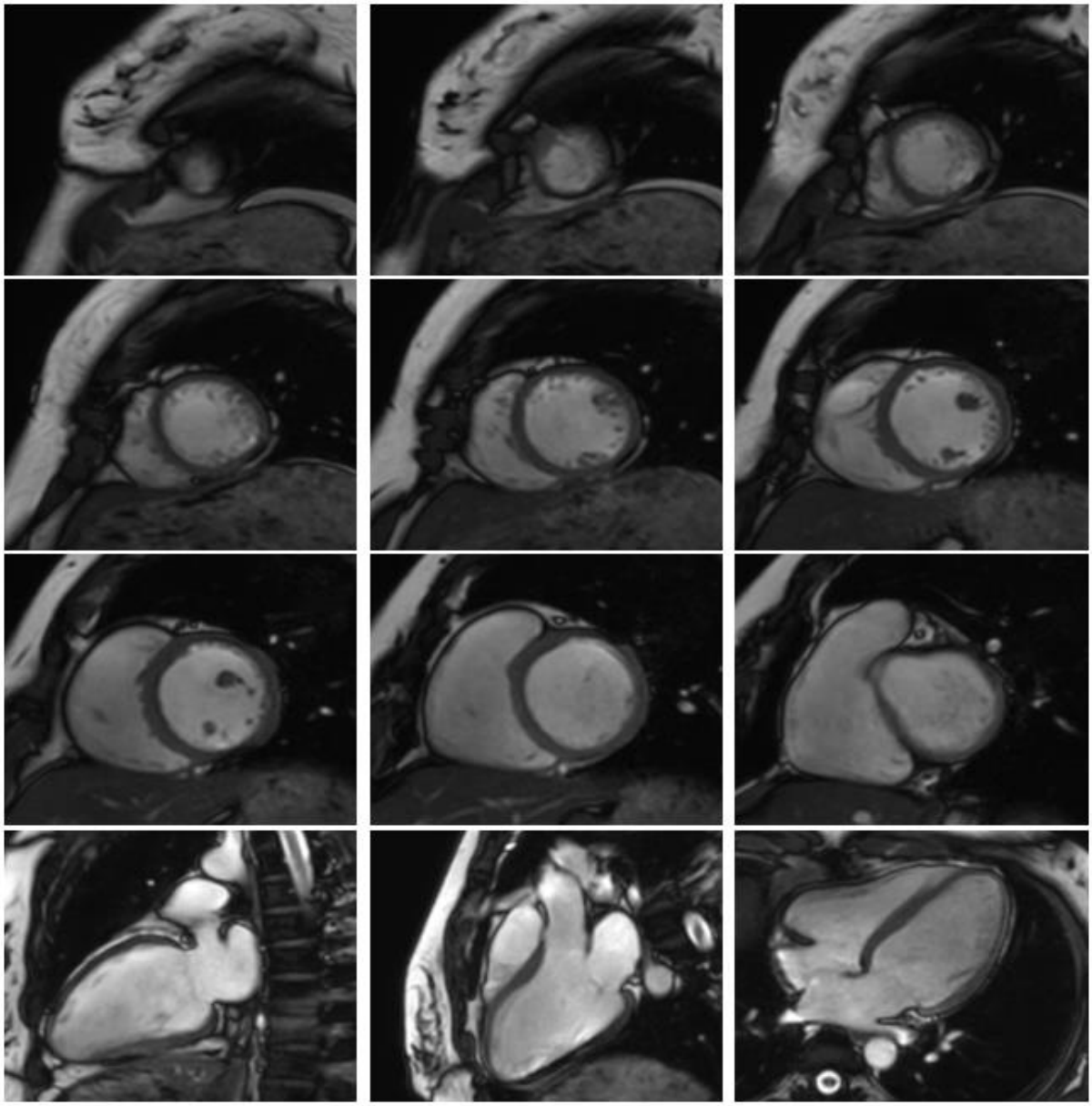

Figure 1. CMR images including short-axis images from apex to basal, and 2-, 3- and 4-chamber long-axis images.

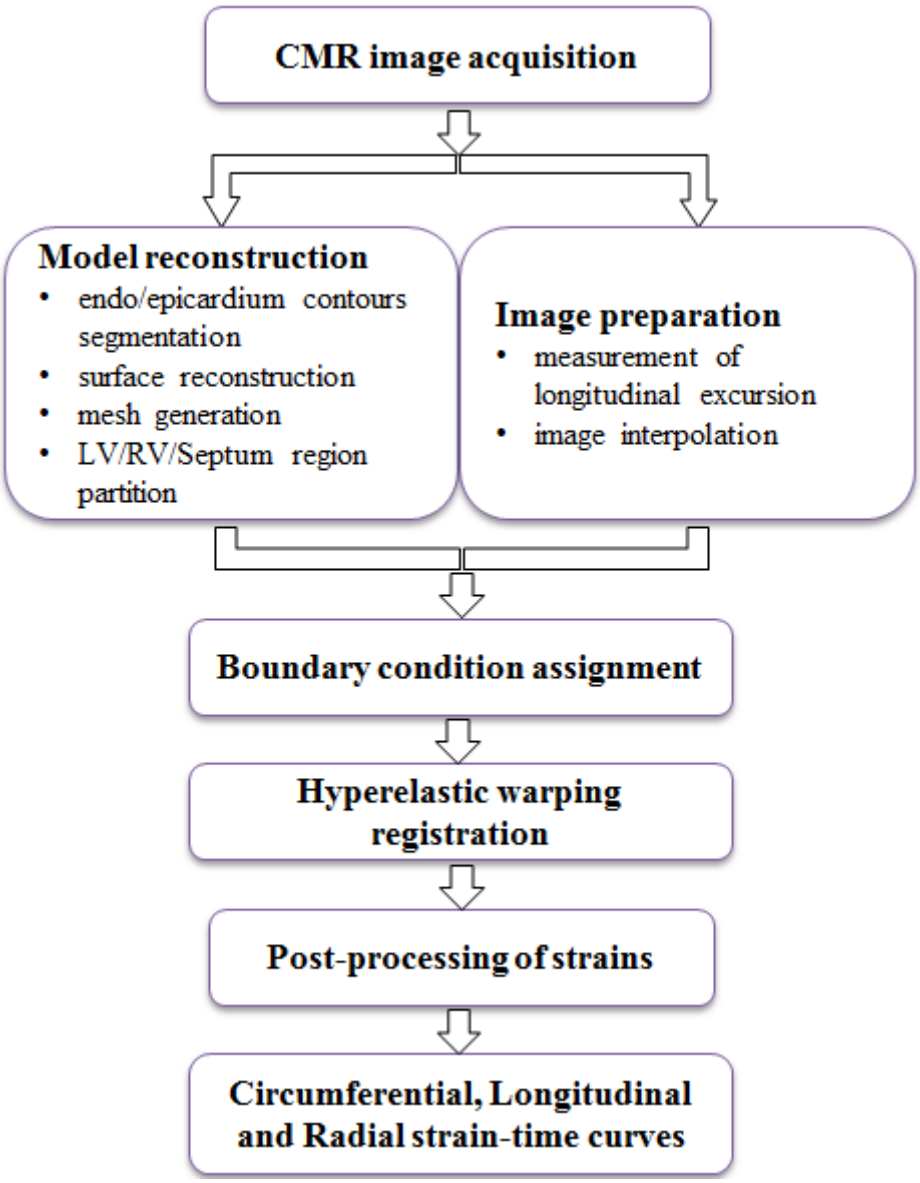

Figure 2. Overall framework of quantifying the biventricular circumferential, longitudinal and radial strains.

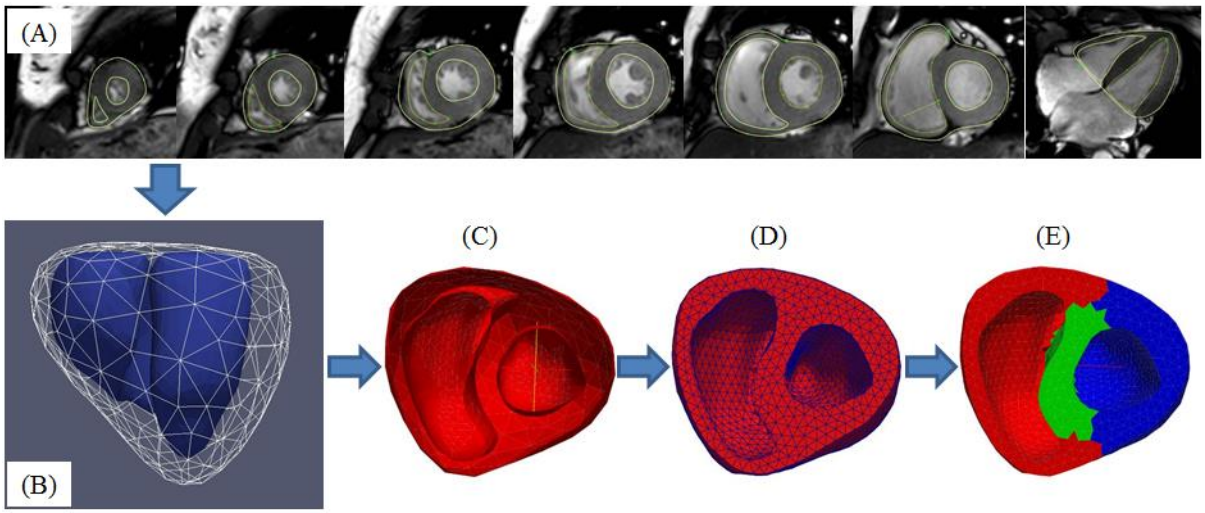

Figure 3. Reconstruction of biventricular mesh: (A) segmentation of contours of LV, RV and septum; (B) Surface reconstruction; (C) Biventricular geometry (D) Biventricular mesh; (E) Partition of region (Red: right ventricle; Green: septum; Blue: left ventricle).

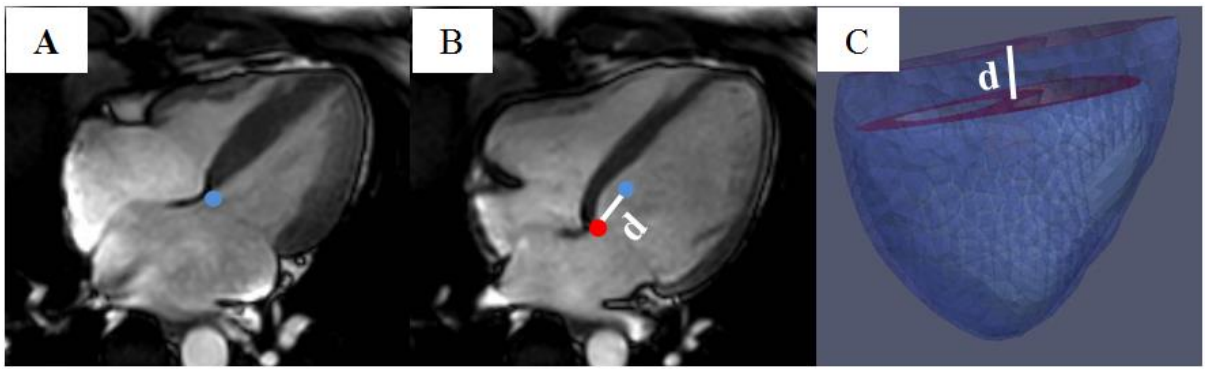

Figure 4. Measurement of the septal displacement in 4-chamber view as the boundary condition: (A) End-systole; (B) End-diastole; (C) Apply the displacement of septal on the model.

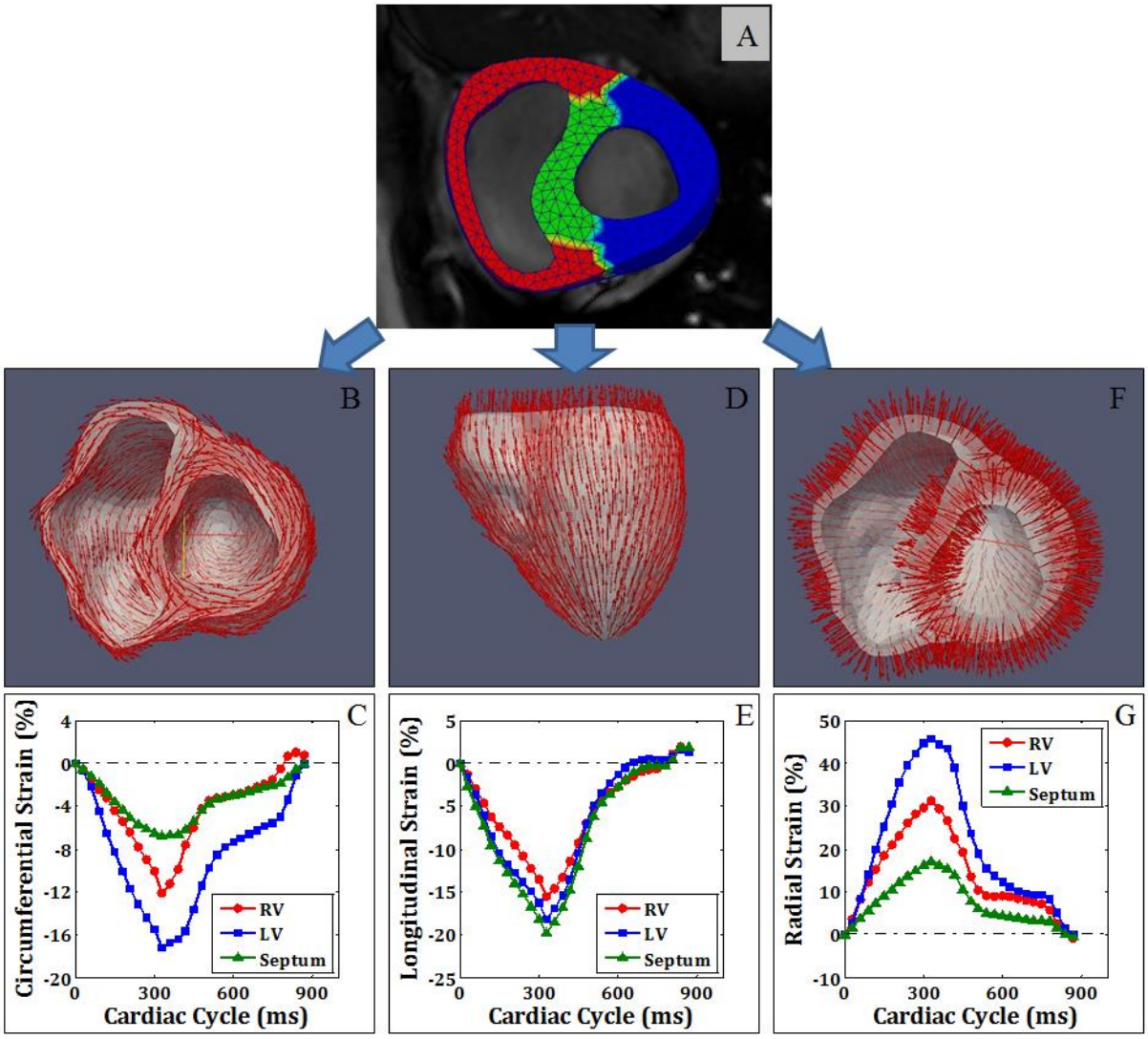

Figure 5. Registration of the meshed model with images for strain-time curves (A) meshed model with CMR image; (B) circumferential strain orientation; (C) circumferential strain-time curve; (D) longitudinal strain orientation; (E) longitudinal strain-time curve; (F) radial strain orientation; (G) radial strain-time curve.

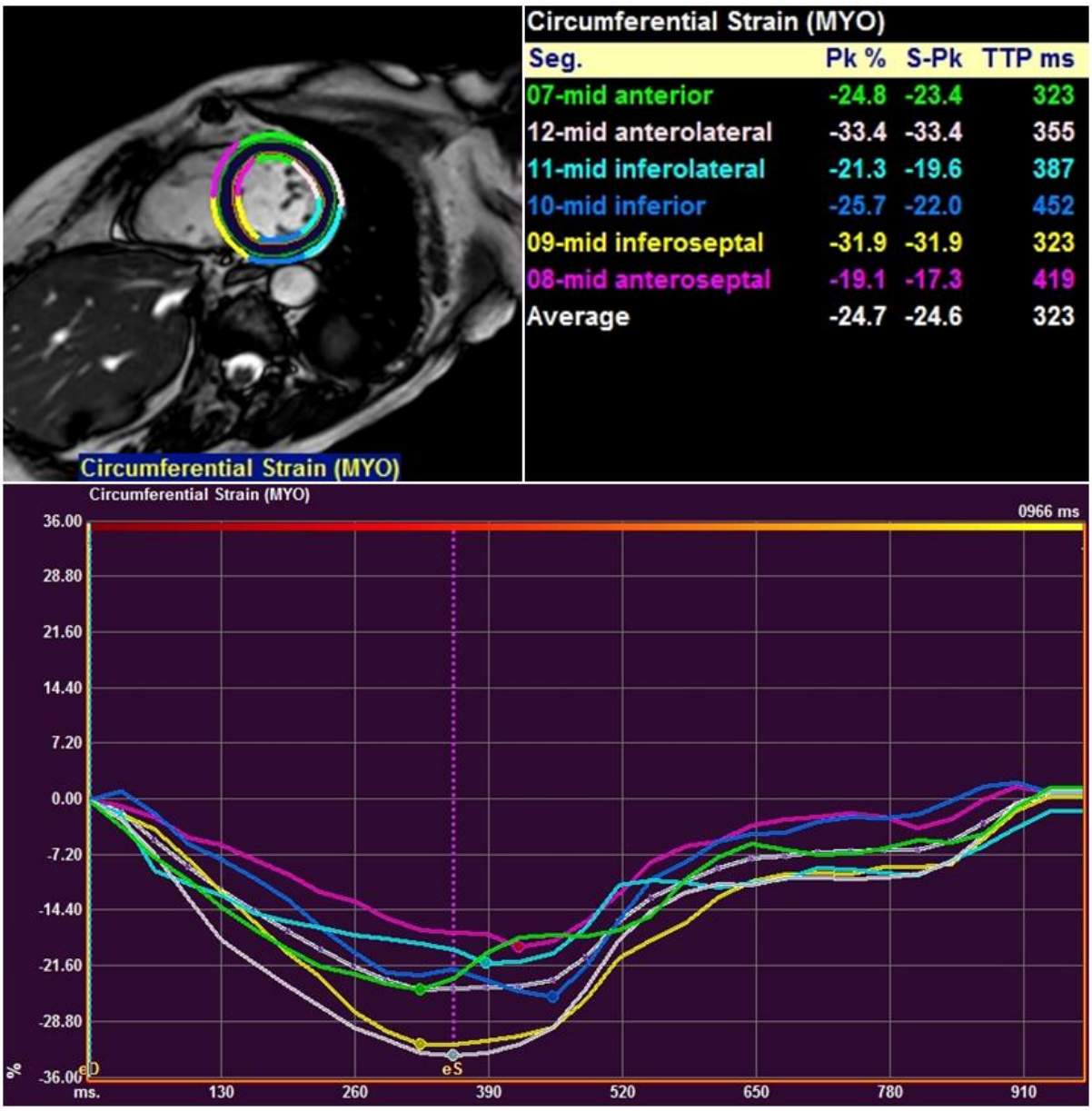

Figure 6. Regional circumferential strain for middle short-axis slice by two-dimensional feature tracking.